Elastic properties of MgO nanocrystals and grain boundaries at high pressures by Brillouin scattering

H. Marquardt,[1,*] A. Gleason,[2,†] K. Marquardt,[1] S. Speziale,[1] L. Miyagi,[3] G. Neusser,[4] H.-R. Wenk,[2] and R. Jeanloz[2]

[1]*German Research Center for Geosciences (GFZ), Telegrafenberg, 14473 Potsdam, Germany*

[2]*Department of Earth and Planetary Science, University of California, Berkeley, California 94720*

[3]*Geology and Geophysics Department, Yale University, P.O. Box 208109, New Haven, Connecticut 06520*

[4]*Institute for Geological Sciences, Freie Universität Berlin, 12249 Berlin, Germany*

Intercrystalline materials (mostly grain boundaries) constitute a substantial fraction of the volume in nanomaterials and significantly influence the material's elasticity, as well as other physical and chemical properties. The effective elastic behavior of intercrystalline material is poorly understood at room pressure and unknown at elevated pressures. Here, we measured acoustic wave velocities of nanocrystalline MgO to pressures of 30 GPa by Brillouin scattering at room temperature. We estimate that both the zero-pressure bulk and shear moduli of the intercrystalline material ($K_{0,IC}$ and $G_{0,IC}$) are reduced by at least 50% compared with the crystalline material. We show that this profound reduction in elastic moduli is preserved at high pressures. Sample characterization as a function of pressure by synchrotron x-ray diffraction shows that the average crystallite size stabilizes to 7 ($\pm$1) nm at high pressure. The microstructure of the sample material after compression was analyzed by high-resolution transmission and scanning electron microscopy. The implications of our observations for the interpretation of Brillouin scattering results from polycrystalline materials are discussed.

I. INTRODUCTION

Nanomaterials with crystallite sizes less than 100 nm can exhibit markedly different physical and chemical properties compared with their bulk (micrometer-sized or larger) counterparts (e.g., Refs. 1–7) because of their different properties and the relatively large fraction of intercrystalline material. Our understanding of the effects of crystallite size on bulk elastic properties is, however, only fragmentary, particularly at high pressure. Yeheskel *et al.*[7] studied the propagation of ultrasonic sound waves through a large number of sintered MgO ceramics, with crystallite sizes between 23 and 114 nm at room pressure. They report a general decrease in acoustic-wave velocities and elastic moduli with decreasing crystallite size, once the crystallite size is sufficiently small for inter-crystalline material to gain influence. This study, however, was limited to relatively "large" crystallites at room pressure. Previous high-pressure studies,[8–10] using synchrotron x-ray diffraction on nanocrystalline powders, mainly probed the crystalline cores because the photon wavelength is typically less than 0.1 nm. X-ray diffraction, therefore, does not necessarily document the bulk properties of nanomaterials. Additionally, x-ray diffraction does not measure the materials' shear properties.

Here, we have used high-pressure Brillouin scattering on nanocrystalline (nc-) MgO powder to derive both bulk and shear moduli and their respective pressure derivatives. In Brillouin spectroscopy, the material is probed by visible light that is scattered inelastically by thermal acoustic vibrations in the sample, with a wavelength of a few hundred nanometers (the exact value depends on the laser wavelength and scattering geometry). The sizes of the nanocrystals are nearly two orders of magnitude smaller than the incident wavelength, and the Brillouin signal represents an average over crystalline and intercrystalline (mostly grain boundary) material. For our high-pressure experiments, nc-MgO powder was pressurized in a diamond-anvil cell. We combined the information from the line broadening observed in a complementary high-pressure synchrotron x-ray diffraction experiment (in radial geometry[11]) with the direct determination of crystallite and particle size obtained from high-resolution secondary electron microscopy (HRSEM) and high-resolution transmission electron microscopy (HRTEM) to characterize our starting powder and to monitor the pressure-dependent evolution of particle and crystallite sizes. The x-ray diffraction data collected in the radial direction provide us with additional information about the crystals' preferred orientation and information about the stress field in the diamond-anvil cell.

II. MATERIAL AND METHODS

Commercially available MgO powder (American Elements, MG-OX-03-P, 99.9%; stated particle size 1 μm, verified by gas absorption BET analysis) was used as starting material for all the high-pressure experimental runs. The average crystallite size of the starting material was about 20 nm (see Discussion for more details on the particle/crystallite size).

A. Brillouin spectroscopy

Brillouin scattering was performed using two different systems (a) at the Advanced Light Source (ALS), Lawrence Berkeley National Laboratory, and (b) at the German Research Center for Geosciences (GFZ). Both systems use a solid-state laser with a wavelength of 532 nm as light source and a multipass tandem Fabry–Perot Interferometer.[12] The system at the ALS is equipped with a photodiode detector, and the external scattering angle was set to 70° (in symmetric forward geometry). The GFZ instrument uses a photomultiplier tube for signal detection, and the measurements were performed in 60° symmetric forward-scattering geometry or in symmetric

90° reflection geometry (cf. Ref. [13]). In forward scattering, the probed phonon wave-vector is perpendicular to the compression direction, whereas in reflection geometry, it is in the direction of compression. A combination of both geometries gives information about the effect of uniaxial stress on the wave velocities. The refractive index, which is required to determine sound wave velocities measured in reflection geometry, was derived from Ref. [14]. Repeated measurements were performed at selected pressures, modifying the incident beam polarization but without analyzing the polarization of the scattered light. The size of the focused laser spot was about 15 μm in diameter, and the focal depth was larger than 25 μm.

Either a symmetric diamond-anvil cell or a BX-90 cell[15] was used. Diamonds with 300-μm culet sizes were employed, along with gaskets made of either stainless steel or boron-epoxy mixture in 4:1 weight ratio. The steel gaskets were pre-indented to thicknesses between 20 and 35 μm, and the initial diameters of the sample chambers varied between 80 and 150 μm. Two or more ruby spheres were loaded in the sample chamber along with the nc-MgO powder to monitor pressure. No ruby was loaded in one experimental run, in which x-ray diffraction in radial geometry was performed to complement the Brillouin scattering data. In this experiment, pressure was calculated from the equation of state of MgO.[16] The unit-cell parameter of MgO was determined by analyzing only the region of the Debye rings at 54.7° from the compression direction (cf. Ref. [17]). The strain measured at this angle corresponds to the hydrostatic component of the stress field applied to the sample.[18] Most experiments were performed without any pressure-transmitting medium. One experiment was conducted using NaCl as the pressure-transmitting medium: in this experiment, nc-MgO powder was sandwiched between two prepressed layers of NaCl powder having initial thicknesses of about 5 μm.

B. Radial x-ray diffraction

Synchrotron x-ray diffraction experiments were carried out at Beamline 12.2.2 of the ALS. A monochromatic beam with an energy of 35 keV was used. nc-MgO powder was loaded in a x-ray transparent gasket made of a boron-epoxy mixture, surrounded by a Kapton ring.[19] The initial gasket thickness was about 50 μm, and the sample chamber had a diameter of about 80 μm. A BX-90 diamond-anvil cell[15] and diamonds with culet sizes of 300 μm were used to pressurize the sample. This cell was originally designed for Brillouin scattering and axial x-ray diffraction experiments. However, it has lateral openings of sufficient size to allow x-ray diffraction experiments in radial geometry and Brillouin scattering measurements on the same loading. We analyzed the x-ray diffraction data, collected with a MAR 345 image plate detector, for texture, axial compressive stress, grain size, and microstrain using a Rietveld full-spectrum fitting method implemented through the program MAUD.[20] Crystallite size was extracted using an isotropic size strain model and Popa line broadening.[21] Instrument peak broadening was corrected using data from a LaB$_6$ standard. The moment pole stress model[22,23] was used to refine elastic lattice strains and calculate stresses. Single-crystal elastic constants of MgO[24] at the corresponding pressures were used as input parameters. The stress tensor

was constrained to account for the geometry of radial x-ray diffraction experiments in the diamond cell. A bulk path geometric mean[23] was assumed for the micromechanical model, which lies between the Voigt and Reuss bounds. The moment pole stress model is similar to that of Refs. [18] and [25] but can be applied to more complicated deformation geometries and accounts for the effects of preferred orientation.

Using the method of Ref. [26], crystallite size was also calculated from the broadening of the (200) and the (220) diffraction rings at 54.7° from the compression direction after correcting for instrumental broadening. Uncertainties in average crystallite size are estimated by taking into account the differences in results between the two methods used in this study.

C. Scanning electron microscopy

Decompressed gaskets were removed from the diamonds and sputtered with carbon for SEM analysis. We used a FEI Quanta 3D at the Free University in Berlin that is equipped with a Field Emission Gun for high spatial resolution. The machine was operated at 5 and 20 kV acceleration voltage, achieving a point resolution better than 5 nm.

D. Transmission electron microscopy

Electron-transparent lamellae for TEM (15 × 8 × 0.10 μm^3) were prepared using the focused ion beam (FIB) technique.[27–30] We used a Tecnai F20 X-Twin TEM operated at 200 kV equipped with a field emission gun as electron source. The microscope has a high-angle annular dark field detector, and an EDAX energy-dispersive spectrometer for x-ray detection in scanning TEM mode. The attached postcolumn Gatan imaging filter (GIF Tridiem) allows for energy-filtered imaging, and the zero-loss peak was limited by a 10-eV window. Electron diffraction patterns were obtained by Fourier transform using the Gatan Digital Micrograph software, where the ring mask method was used to prevent lattice fringe extrapolations.[31,32]

III. RESULTS AND DISCUSSION

A. Crystallite/particle size

Our HRSEM analysis shows that the starting material consists of agglomerates with a diameter of about 1 μm [Figs. 1(a) and 1(b)], consistent with what is stated by the supplier based on gas absorption measurements. However, those agglomerates are not single-crystalline but consist of a number of smaller rounded bodies with significantly smaller diameter [69 ± 11 nm; Fig. 1(c)]. We chose to refer to these roundish bodies as "particles," because it cannot be judged from SEM images whether they are single crystals or clusters of crystals.

We systematically characterized the final particle size of all our experiments after decompression. The average diameter of 50 particles (chosen arbitrarily) was visually estimated from SEM images and used to calculate the arithmetic mean diameter and the corresponding standard deviation (1σ). Upon compression, the agglomerates break apart and a material with relatively homogenous particle size (58 ± 11 nm) is produced
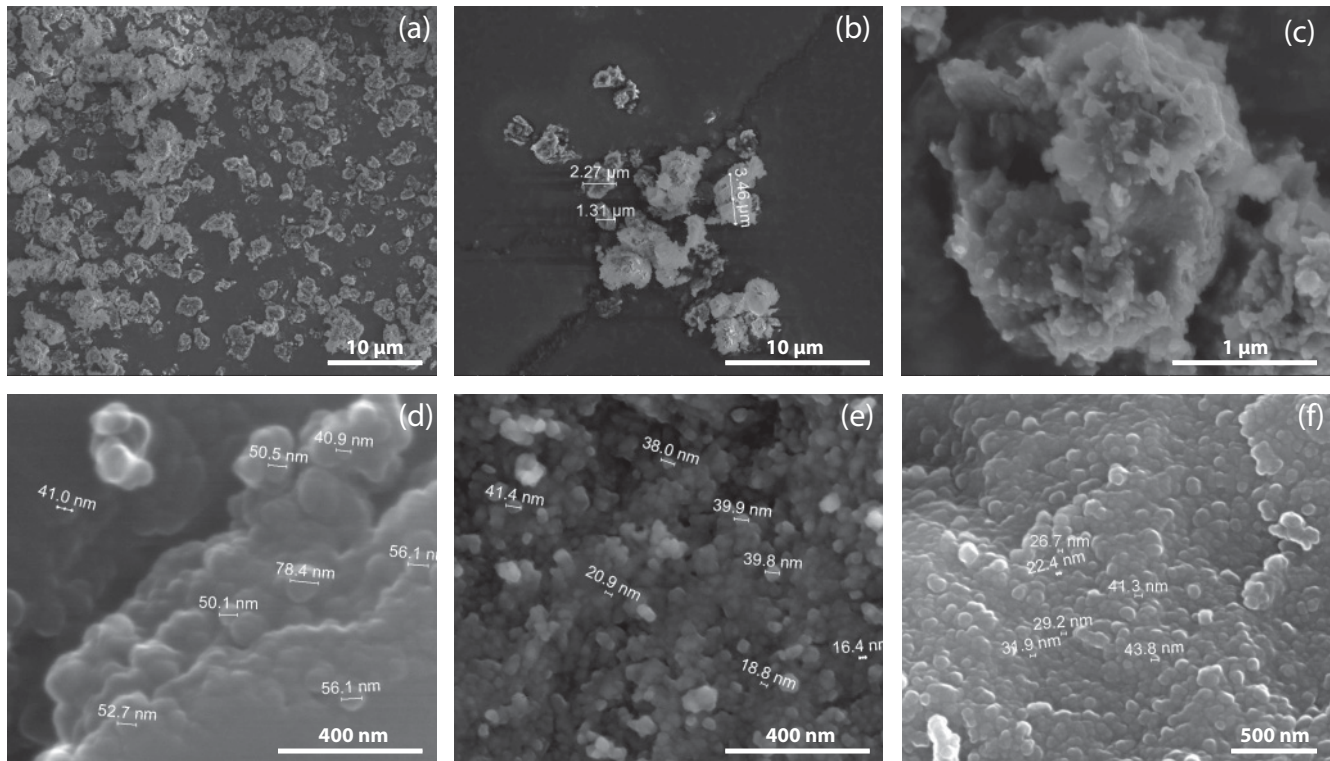
FIG. 1. HRSEM characterization of the particle size of MgO starting material and decompressed run products. (a)–(c) The MgO starting material consists of rounded agglomerates with a mean diameter of approximately 1 μm, composed of a number of particles (see main text) with average diameter of 69 ($\pm$11) nm [magnification is $\times$6500 (a), $\times$10,000 (b), and $\times$100,000 (c)]. (d)–(f) Recovered samples after decompression from 1.2 GPa (d), 4.6 GPa (e), and 31.3 GPa (f). The large plane area in the lower right corner of panel (d) corresponds to the contact area between sample and diamond.

after compression to 1.2 GPa [Fig. 1(d)]. A sample that was compressed to 4.6 GPa shows a slightly smaller average particle size of 37 ($\pm$9) nm [Fig. 1(e)]. Within uncertainties, this sample shows about the same mean particle size as the run product of the 31.3 GPa run [43 $\pm$ 9 nm; Fig. 1(f)], indicating that the particle size stabilizes above roughly 5 GPa.

We performed a detailed analysis of a sample recovered from 22.4 GPa using TEM (Fig. 2). This analysis revealed that the particles observed by SEM consist of several crystallites (single crystal grains). The scanning TEM (STEM) image gives an overview of the lamella that was cut from the recovered sample using a FIB [Fig. 2(a)]. The upper left part of the lamella broke during sample preparation, and the red square highlights the region that is enlarged in Fig. 2(b). At the surface of the crack [Fig. 2(b)], one observes the same foam structures visible in the SEM images [Figs. 1(d)–1(f)]. Those structures are likely caused by clustering of crystallites to reduce the surface area. Figure 2(c) is another representative STEM image, in which the contrast is generated by both mass difference and difference in crystallographic orientation. The large elliptic structures on the bottom right are artifacts from the underlying carbon grid. Brighter parts of the image correspond to crystallites. Figure 2(d) shows a bright field image of a representative part of the sample. The dark spots in this image correspond to crystallites. When changing the diffraction conditions by sample tilting, the dark spots changed place, but the overall picture was retained. The large

bright features are likely caused by fracturing of the material upon decompression. Figures 2(c) and 2(d) illustrates the small crystallite size of our sample material. To quantify the crystallite sizes, we took HRTEM images at selected regions of the TEM lamella. Figure 3(a) shows a representative example. The mottled structure is related to amorphous material, which might be either an effect of sample preparation or an intrinsic material property. Upon tilting the sample, we could observe several lattice fringes that belong to different crystallites [highlighted in Fig. 3(a)]. Moiré patterns can be observed in some regions of the image [Fig. 3(a)]. Those features are related to superimposed crystalline structures that generate an additional periodic structure with larger spacing. A diffraction pattern was generated by a Fourier transform of the entire image and is shown in Fig. 3(b). The diffraction rings that correspond to the (111), (200), and (220) lattice planes are labeled. The bright diffraction spots that appear close to the center of the pattern are related to moiré patterns. On the basis of HRTEM images taken at various positions in the decompressed sample material, the average crystallite size was determined to be 6.9 ($\pm$1.5) nm. This number represents the arithmetic mean value ($\pm$1σ-standard deviation) of 100 crystallites, where their size was visually estimated from the spatial extent of the lattice fringes. This finding is in excellent agreement with the crystallite size determination from the x-ray line broadening, in which an average crystallite size of 7 ($\pm$1) nm was deduced at high pressures. The average
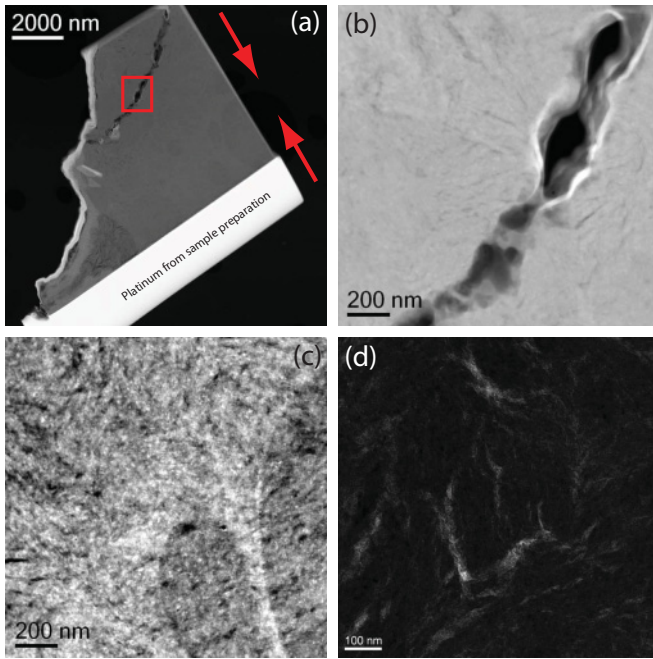
FIG. 2. (Color online) (a) STEM overview of a lamella for TEM observations cut by the focused ion beam (FIB) technique. The lamella was cut parallel to the compression direction (indicated by red arrows) and extends to roughly half of the sample's thickness. (b) Enlarged view of the region highlighted in panel (a). Agglomerates of MgO crystals are visible at the crack's surface, comparable to the particles observed in the SEM images [Figs. 1(d)–1(f)]. (c), (d) STEM and bright field images of selected areas of the same sample.
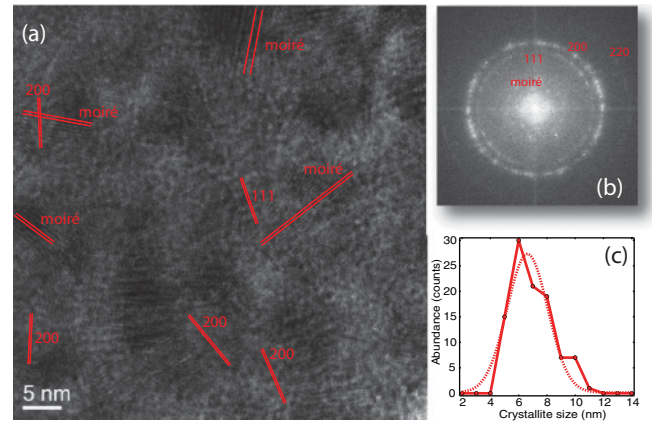

FIG. 3. (Color online) TEM analysis of a sample decompressed from 22.4 GPa. (a) Representative HRTEM image. Red lines illustrate the spatial extent of several lattice fringes. (b) A diffraction pattern was generated by Fourier transform of the entire image (the thickness of the TEM foil is about 100 nm). (c) Crystallite size distribution as derived from visual evaluation of 100 crystallites (in several HRTEM images at selected regions of the FIB-TEM lamella, see also Fig. 2). A Gaussian fit to the crystallite size data is shown as dotted curve.

crystallite size of the starting material was determined to be around 20 nm on the basis of x-ray line broadening analysis and HRTEM. Figure 4 illustrates the observed variation of particle and crystallite sizes with increasing pressure. After an observable reduction upon initial compression, both particle and crystallite size stabilize at pressures greater than ~5 GPa. Our findings imply that HRSEM cannot resolve single crystallites in a material with very small crystallite size but images clusters of crystallites that form on the surface, likely as a result of energy minimization.

B. Sound wave velocities

The sound velocities that we observe for nc-MgO powder are significantly lower than expected from single-crystal data for MgO[33] (Fig. 5). It was also found in all experiments that the aggregate Poisson ratio, $\sigma = 1/2(v_p^2 - 2v_s^2)/(v_p^2 - v_s^2) = (3K - 2G)/(6K + 2G)$—where K is the bulk modulus, and G is the shear modulus—is significantly increased compared with the single-crystal reference value (Fig. 5).

In our experiments, we systematically find a significant change in relative amplitudes of the signals from shear and compressional wave velocities. We could not detect any significant signal related to the shear wave at around 1 GPa, in which the nc-MgO powder becomes optically translucent and Brillouin measurements could be performed. There was, however, a strong contribution from the compressional wave. With increasing pressure, the shear-wave signal became
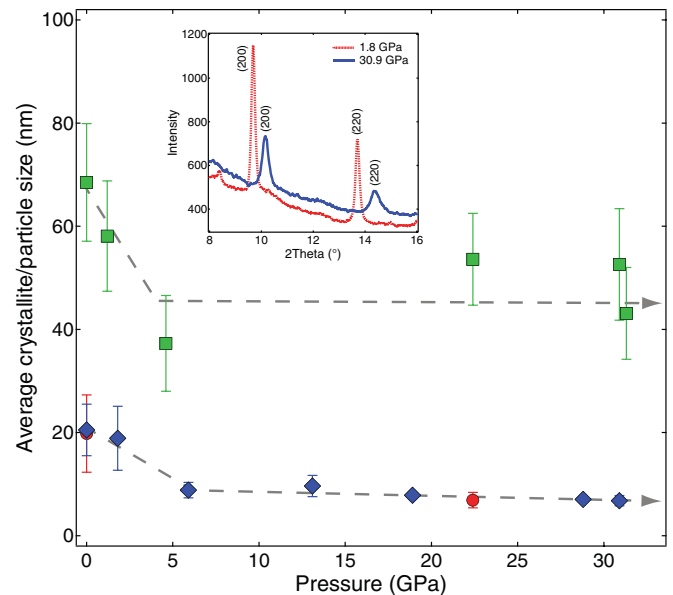

FIG. 4. (Color online) Reduction of particle and crystallite size as a function of experimental pressure. Green squares: average particle size estimated by HRSEM imaging of decompressed samples (arithmetic mean diameter of 50 particles with error bars corresponding to 1σ standard deviation). Blue diamonds: crystallite size determined from the broadening of the x-ray diffraction peaks (the error bars take into account the results from two different approaches, see text for details). The red circles refer to the mean crystallite size estimated from TEM analysis of a decompressed sample (arithmetic mean of 100 crystallites with 1σ standard deviation) and the starting material (arithmetic mean of 15 crystallites). The inset shows diffraction patterns taken at 1.8 GPa and 30.9 GPa, illustrating the x-ray line broadening caused by microstrains and a reduction of the average crystallite size from 19 (± 6) nm at 1.8 GPa to 7 (± 1) nm at 30.9 GPa.
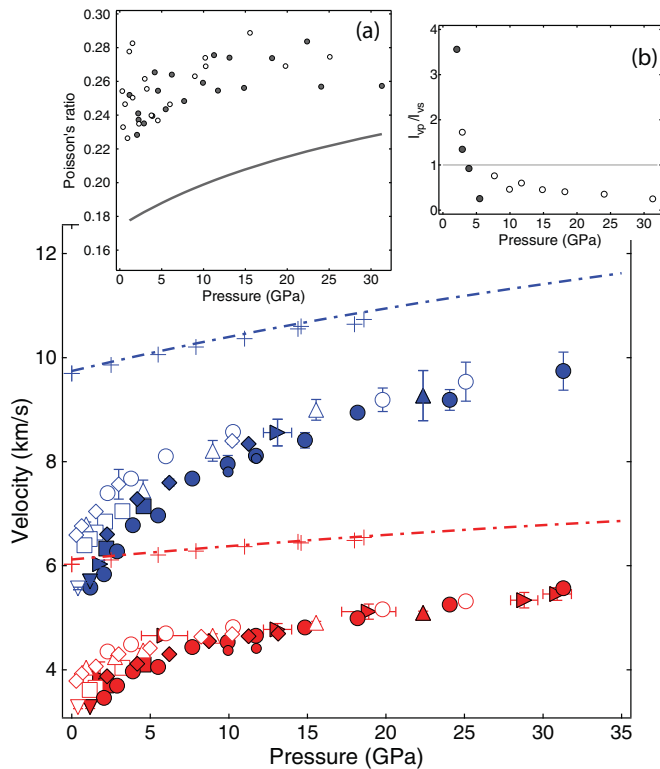
FIG. 5. (Color online) Pressure dependence of compressional (blue) and shear (red) velocities of nc-MgO powder. Filled symbols: data collected in compression. Open symbols: decompression data. Different symbols represent different experimental runs. Diamonds: data set measured with NaCl as pressure-transmitting medium. Small filled circles: velocities measured in reflection geometry[13] (i.e., along the compression direction). Crosses are Voigt–Reuss–Hill average velocities from single-crystal experiments[33] assuming a random orientation distribution. Dash-dotted curves: computational results[24]. Inset (a): Poisson ratio of nc-MgO as a function of pressure. The Poisson ratio of "bulk" MgO[24] is shown as a solid curve for comparison. Inset (b): Ratio of amplitudes of Brillouin signal for compressional and shear mode. Full circles: polarization of incoming laser light is vertical. Open circles: polarization of incoming laser light is horizontal (both light wave vector and acoustic wave vector are in the horizontal plane in our experiments).

stronger, whereas the contribution of the compressional wave decreased. The relative change in the observed amplitudes is illustrated in Fig. 5(b). Above 6 GPa, the longitudinal mode was not detectable anymore, but it re-appeared after rotating the polarization of the incoming laser light by 90°. Hysteresis also appears at low pressures, with the velocities measured on decompression being higher than those collected at the same pressure on compression. It appears that decompression from higher pressures results in higher velocities, compared with data collected on decompression from lower peak (maximum) pressures; the higher the maximum experimental pressure, the higher the decompression data in velocity. However, velocities measured on decompression are still significantly less than those reported for single-crystal MgO.

On the basis of our observations, we distinguish two major pressure regimes during compression. At pressures less than 6 GPa, crystallite size reduction takes place and the material is in a transient mechanical state—manifested by extremely low velocities and changes of intensity ratios between compressional and shear mode; this can even be observed as a change of the sharpness of the laser-focus spot in the sample. At pressures larger than 6 GPa, the crystallite size remains almost constant, and the sample appears to be in mechanical equilibrium, as indicated by the observed hysteresis.

In one loading, nc-MgO powder was sandwiched between two layers of pre-pressed NaCl powder that serve as a pressure-transmitting medium. We find the same low velocities for MgO as in the experiments without NaCl at all experimental pressures but observe velocities for NaCl that are in agreement with previously published data for single crystals[34] (a typical spectrum is shown in Fig. 6). A subsequent HRSEM analysis showed that NaCl preserves crystallite sizes larger than 1 μm (appearing as small cubes in Fig. 6), confirming that the Brillouin frequency shifts are directly influenced by the small crystallite sizes of the nc-MgO powder.

C. Texture/nonhydrostaticity

Most of our experiments were carried out under nonhydrostatic conditions, and it is important to evaluate any potential bias of the derived sound wave velocities by the nonuniform stress distribution and a potential associated preferred orientation of the crystallites. We therefore complemented one of our experimental runs with data collected by radial x-ray
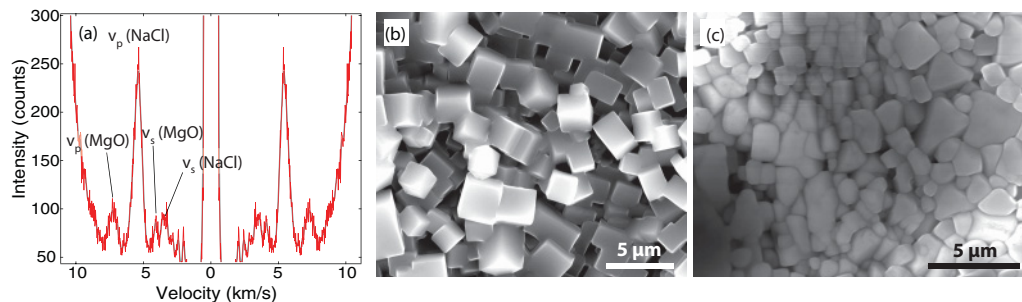

FIG. 6. (Color online) (a) Brillouin spectrum collected at 4.2 GPa in the experimental run in which MgO powder was sandwiched between layers of NaCl. The respective peaks are labeled. (b), (c) Average crystallite sizes (arithmetic mean of 50 crystallites) of NaCl are 1633 ($\pm$477) nm after decompression from 4 GPa (b) and 1066 ($\pm$371) nm after decompression from 13.1 GPa (c). NaCl has crystallite sizes of sufficient size for measured Brillouin frequency shifts to represent bulk NaCl.

diffraction on the same loading, which allows us to quantify the uniaxial stress component and detect any preferred orientation at high pressure.

In our experiments, the pressure-dependent uniaxial stress component increases with pressure, reaching a maximum of around 8 GPa at a pressure of 30 GPa. These results are in good agreement with previous radial x-ray diffraction studies on MgO.[17]

The potential effect of nonhydrostaticity on acoustic wave velocities in MgO has been discussed previously.[35] Non-hydrostaticity can, in principle, lead to lower velocities in the plane perpendicular to the maximum principal stress. However, the maximum possible reduction in shear wave velocities is calculated to be 5% at a pressure of 20 GPa, assuming a uniaxial stress of 6 GPa.[35] In our experiments at this pressure, we find the uniaxial stress component to be 6 GPa but observe a reduction of 27% in shear-wave velocities compared with the single-crystal reference.[33] Our direct measurements of deviatoric stresses and sound velocities therefore confirm the previous[35] conclusion that nonhydrostatic effects do not account for the observed reduction in velocities for polycrystalline MgO.

In addition to the results from combined radial x-ray diffraction and Brillouin scattering, the velocities measured by using a reflection geometry (i.e., with the wave vector of the probed phonon parallel to the compression direction) are in agreement with the velocities measured in the same run in transmission geometry (i.e., with the wave vector of the probed phonon perpendicular to the compression direction). Second, the experimental run in which NaCl was employed as the pressure-transmitting medium gives the same low velocities for MgO as found without any pressure-transmitting medium (Fig. 6).

We did not observe any significant texture, even at the highest pressure. This finding is not in agreement with previous studies on the deformation of MgO to high pressure, which document a significant (100) texture (i.e. the {100} lattice planes were aligned perpendicular to the compression direction).[17] Acoustic velocities from Brillouin spectra collected from the same loading, in which we did not detect any significant texture by x-ray diffraction are in complete agreement with all the rest of our dataset; therefore, we conclude that texturing is not causing the observed low velocities (it does not bias our experimental results). Furthermore, the elastic anisotropy of MgO decreases monotonically with pressures vanishing at pressures near 20 GPa and becoming negative at higher pressures[24,33,36]; thus, there cannot be any bias of wave velocities because of texturing at this pressure, yet we measure low velocities, reinforcing the conclusion that texturing does not cause the observed low velocities.

D. Density and elastic moduli

From the measured shear $v_s = (G/\rho)^{0.5}$ and compressional $v_p = [(K + 4/3G)/\rho]^{0.5}$ velocities, we can directly calculate the quantity K/ρ. Taking into account the definition of the bulk modulus (and neglecting the small difference between isothermal and isentropic bulk modulus), it follows that $K/\rho = dP/d\rho$, such that $d\rho$, hence density, of nc-MgO can be calculated from our data at high pressure if the zero-pressure density is known.

In a previous study of sintered nanocrystalline MgO,[7] the density of the intercrystalline phase was estimated to be 3.087 g/cm^3. Here, we use this value to calculate the zero-pressure density that corresponds to the compacted sample. The overall volume fraction of the intercrystalline components f_{ic} and crystallites f_c in a nanomaterial can be calculated from the average grain size and the grain-boundary thickness (e.g., Refs. 37 and 38). Using the model of Ref. 37, which implies a tetrakaidecahedron grain morphology, and assuming a grain boundary thickness of 1 nm, we calculate f_{ic} to be 0.44 for a crystallite size of 7 nm. Here, f_c refers only to the crystalline cores, excluding the grain boundary region, whereas f_{ic} represents all the remaining intercrystalline material, including grain boundaries, triple lines, and quadruple nodes. On the basis of this model and the intercrystalline material's density data of Ref. 7, we derive a density of 3.37 g/cm^3 for compacted nc-MgO with a mean crystallite size of 7 nm.

The evolution of densities with pressure, as derived from the procedure outlined above, is summarized in Fig. 7. On the basis of our previous discussion, we only used the decompression data collected in the highest pressure run (open circles in Fig. 5) because these are most representative of a fully compacted, mechanically equilibrated nc-MgO powder with an average crystallite size of 7 nm. Note that the densities
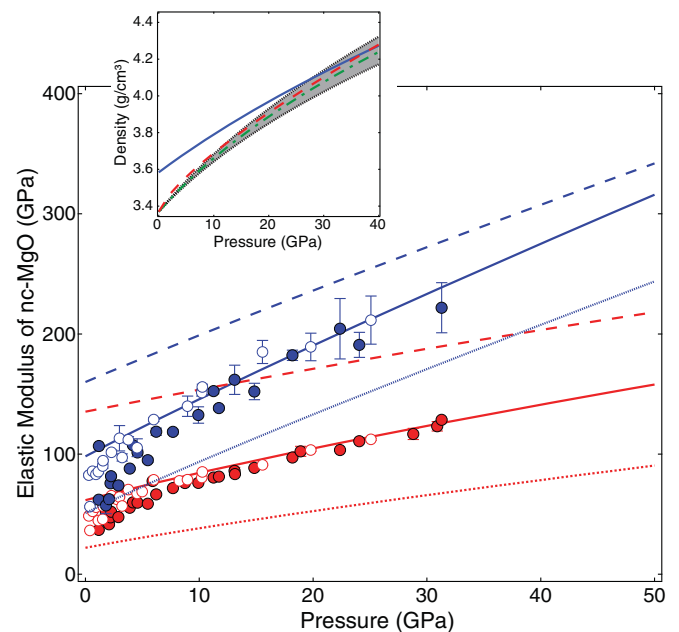

FIG. 7. (Color online) Aggregate elastic moduli of nc-MgO at high pressures. The shear modulus is plotted in red, the bulk modulus in blue. Open circles: data collected on decompression. Solid lines: eulerian finite strain fit of the decompression data collected in the run with the highest peak pressure (including the highest pressure compression datum). Dashed curves: computational results for bulk MgO[24]. Dotted curves: effective elastic moduli of intercrystalline material. The inset shows the variation of density with pressure. Green dashed-dotted curve: third-order Birch–Murnaghan equation of state fit, gray-shaded regions: uncertainty of the fit. Red dashed curve: density from the identity $K/\rho = dP/d\rho$. The starting density was fixed to 3.37 g/cm^3 for both procedures (see main text). Solid blue curve: density of (bulk) single-crystal MgO calculated using the parameters of Ref. 16.

derived by this procedure are not reliable outside the pressure range covered by our experimental data because $\rho/K(P)$ was approximated by a polynomial fit to the data to integrate for ρ.

In a second approach, it was assumed that the data can be described by a third-order Birch–Murnaghan equation of state. The zero-pressure density was again fixed to 3.37 g/cm^3, and the high-pressure densities were derived using an iterative procedure (cf. Ref. [39]) based on a third-order Eulerian finite strain formalism.[40] The results of both procedures agree within mutual uncertainties, and we find that the density of the nc-MgO approaches the single-crystal density at about 30 GPa (Fig. 7).

Knowledge of the high-pressure densities also yields bulk and shear moduli for nc-MgO at high pressure (Fig. 7). Fits to Eulerian finite-strain equations[41] provide the zero-pressure bulk ($K_{0,NC}$) and shear ($G_{0,NC}$) moduli and their respective pressure derivatives $K'_{0,NC}$ and $G'_{0,NC}$. The best-fit coefficients are $K_{0,NC} = 98.1$ (± 5.4) GPa, $K'_{0,NC} = 5$ (± 0.6), $G_{0,NC} = 61.6$ (± 1.2) GPa, $G'_{0,NC} = 2.5$ (± 0.1), where the uncertainties represent 1σ-standard deviations from the least square fits.

The Voigt–Reuss–Hill[42] average model is used along with the composite model[37] to derive the effective elastic moduli and their pressure derivatives for the intercrystalline material at zero pressure, where reported single crystal elastic moduli for MgO[33] are used for the bulk crystalline material (the cores of the crystallites). With this approach, we find $K_{0,IC} = 51$ (± 6) GPa, $K'_{0,IC} = 4.6$ (± 0.7), $G_{0,IC} = 22$ (± 2) GPa, and $G'_{0,IC} = 1.8$ (± 0.1) (only the uncertainties in the coefficients $K_{0,NC}$, $G_{0,NC}$, $K'_{0,NC}$, and $G'_{0,NC}$ are propagated here). For comparison, the single-crystal elastic moduli of MgO yield $K_{0,SC} = 163.2$ (± 1) GPa, $K'_{0,SC} = 3.83$ (± 0.15), $G_{0,SC} = 130.2$ (± 1) GPa, and $G'_{0,SC} = 2.21$ (± 0.1).[33]

It is important to note that the calculations to derive the elastic properties of the intercrystalline material are based on the assumption that the material consists of tetrakaidecahedron-shaped particles with an average diameter of 7 nm and that the grain boundary width is 1 nm. Also, we estimated the zero-pressure density from a previous study.[7] Table I gives an overview of how the derived elastic moduli depend on the choice of average crystallite size and grain boundary thickness. Even though the results differ significantly, all the models require a reduction of at least 50% in both bulk and shear modulus (compared with the single-crystal values) to match our observations.

Yeheskel et al.[7] analyzed ultrasonic sound wave results on nc-MgO based on Hill's composite model for homogeneous polycrystalline materials and calculated the elastic moduli of the grain boundary assuming a grain boundary thickness of 1 nm. They find the grain boundaries' shear modulus to be 34 GPa and the bulk modulus to be 85 GPa. This is somewhat larger than our estimations. However, Yeheskel et al.[7] studied sintered samples (i.e., materials that exhibit a relaxed structure), whereas we measured nc-MgO powder that was produced by mechanically induced crystallite-size reduction under elevated stress.

Our results indicate that, within the limits of our assumptions, the difference in elastic properties of MgO crystallites and intercrystalline material is pronounced. Furthermore, we find that this difference is preserved to high pressures, particularly for the shear properties (Fig. 7). On the basis of our findings, the elastic properties of nanocrystalline materials can be expected to be largely controlled by the effective elastic moduli of the intercrystalline phase, even at high pressures. Our findings indicate that in polycrystalline materials with crystallite sizes of 500 nm, the elastic moduli can still be reduced by 1%–2%.

TABLE I. Summary of the calculated effective elastic moduli of the intercrystalline phase $K_{0,IC}$ and $G_{0,IC}$ for different values of average crystallite size and grain boundary (gb) thickness. The corresponding fractions of the intercrystalline (IC) phase are also reported.

Model no.	Crystallite size (nm)	gb thickness (nm)	K_{IC} (GPa)	G_{IC} (GPa)	Density (g/cm^3)	Fraction of IC phase
1	5	0.5	36.9	13.0	3.42	0.32
2	5	1	63.4	31.5	3.30	0.57
3	5	1.5	76.8	43.4	3.21	0.75
4	5	2	83.7	50.2	3.15	0.87
5	6	0.5	30.6	9.6	3.45	0.28
6	6	1	57.0	26.0	3.34	0.50
7	6	1.5	71.2	38.4	3.25	0.67
8	6	2	79.6	46.1	3.19	0.79
9	7	0.5	25.9	7.4	3.46	0.24
10	7	1	50.5	21.6	3.37	0.44
11	7	1.5	65.9	33.6	3.29	0.60
12	7	2	75.3	42.1	3.22	0.73
13	8	0.5	22.2	5.8	3.48	0.21
14	8	1	18.1	45.2	3.39	0.39
15	8	1.5	29.6	61.0	3.31	0.54
16	8	2	71.2	38.3	3.25	0.67
17	9	0.5	19.4	4.7	3.49	0.19
18	9	1	40.7	15.2	3.41	0.36
19	9	1.5	56.5	26.0	3.34	0.50
20	9	2	67.2	34.8	3.28	0.61

E. Implications for Brillouin spectroscopy on powders/polycrystals

On the basis of the pronounced difference between crystalline and intercrystalline elastic properties that we observe in the present study, we speculate that Brillouin frequency shifts measured on polycrystals might be biased even at much larger grain sizes. It has been observed that meso-sized particles (i.e., tens to hundreds of nanometers) can exhibit unexpected features in the frequency range probed by Brillouin spectroscopy. It has also been shown in a number of studies that spatial confinement of acoustic phonons can cause the disappearance of bulk acoustic modes and the simultaneous appearance of new features at distinct frequencies in the Brillouin spectra that are related to the eigenvibrations of the crystallites. These features have been observed for single isolated SiO_2 nanospheres,[43] for loose SiO_2 microspheres,[44] and for synthetic opals[45] with diameters between 140 and 515 nm. These considerations could imply that Brillouin scattering experiments on polycrystals that aim at deriving "bulk" elastic properties should be restricted to a narrow range of crystallite sizes around 1–3 μm—small enough to guarantee sufficient statistics in Brillouin scattering experiments and large enough not to suffer from the contribution of nano-/meso-scale properties. The suitable size range likely depends on the material's mechanical properties, including its elastic anisotropy. Our findings provide an explanation for previous Brillouin results on the sound wave velocities of MgO powder compressed under nonhydrostatic conditions, in which velocities were found to be anomalously low.[35]

IV. CONCLUSION

We have carried out Brillouin scattering experiments on nc-MgO powder compressed in a diamond-anvil cell with and without a pressure-transmitting medium. In all experimental runs, we observe sound wave velocities that are significantly lower than expected from single-crystal reference data. We have monitored the evolution of both particle and crystallite sizes with pressure using x-ray diffraction line-broadening analysis, high-resolution SEM, and TEM. Our findings indicate that the average crystallite size reduces on compression to about 7 ($\pm$1) nm. The small average crystallite sizes have profound effects on the elastic properties and are causing the observed low velocities in MgO. We show that this effect prevails at high pressures. On the basis of our data analysis, both bulk and shear modulus of the intercrystalline phase are substantially reduced compared with MgO single-crystal data. By performing a simultaneous analysis of uniaxial stress, texture development, and Brillouin scattering, we demonstrate that the effect of crystallite size on the measured velocities exceeds by far any effects of nonhydrostaticity and texturing. This implies that a thorough characterization of the crystallite size distribution is important for the interpretation of Brillouin scattering results from polycrystalline materials.

*hama@gfz-potsdam.de

†Present address: Department of Geological and Environmental Sciences, Braun Hall, Building 320, Stanford University, Stanford, California 94305-2115.

[1] M. F. Hochella Jr., S. K. Lower, P. A. Maurice, R. L. Penn, N. Sahai, D. L. Sparks, and B. S. Twining, Science **319**, 1631 (2008).

[2] H. Gleiter, Acta Mater. **48**, 1 (2000).

[3] B. Fultz, C. C. Ahn, E. E. Alp, W. Sturhahn, and T. S. Toellner, Phys. Rev. Lett. **79**, 937 (1997).

[4] A. N. Goldstein, C. M. Echer, and A. P. Alivisatos, Science **256**, 1425 (1992).

[5] J. Schiotz, F. D. Di Tolla, and K. W. Jacobsen, Nature **391**, 561 (1998).

[6] V. Pischedda, G. R. Hearne, A. M. Dawe, and J. E. Lowther, Phys. Rev. Lett. **96**, 035509 (2006).

[7] O. Yeheskel, R. Chaim, Z. Shen, and M. Nygren, J. Mater. Res. **20**, 719 (2005).

[8] B. Chen, D. Penwell, L. R. Benedetti, R. Jeanloz, and M. B. Kruger, Phys. Rev. B **66**, 144101 (2002).

[9] H. Dong, D. He, T. S. Duffy, and Y. Zhao, Phys. Rev. B **79**, 014105 (2009).

[10] S. R.Venilla, S. R. Kulkarni, S. K. Saxena, H. P. Liermann, and Sinogeikin, Appl. Phys. Lett. **89**, 261901 (2006).

[11] A. K. Singh, H.-k. Mao, J. Shu, and R. J. Hemley, Phys. Rev. Lett. **80**, 2157 (1998).

[12] J. R. Sandercock, in *Light Scattering in Solids III: Recent Results*, edited by M. Cardona and G. Guntherodt (Springer, Berlin, 1982), pp. 173–206.

[13] H. Marquardt, S. Speziale, S. Jahn, S. Ganschow, and F. R. Schilling, J. Appl. Phys. **106**, 093519 (2009).

[14] B. R. Jovanic, Phys. Scr. **56**, 477 (1997).

[15] I. Y. Kantor, V. Prakapenka, P. Dera, and L. Dubrovinsky, BGI Annual Report 208 (2008).

[16] S. Speziale, C. S. Zha, T. S. Duffy, R. J. Hemley, and H. K. Mao, J. Geophys. Res. B **106**, 515 (2001).

[17] S. Merkel, H. R. Wenk, J. Shu, G. Shen, P. Gillet, H.-k. Mao, and R. J. Hemley, J. Geophys. Res. **107**, 2271 (2002).

[18] A. K. Singh, C. Balasingh, H.-k. Mao, R. J. Hemley, and J. Shu, J. Appl. Phys. **83**, 7567 (1998).

[19] S. Merkel and T. Yagi, Rev. Sci. Instrum. **76**, 046109 (2005).

[20] L. Lutterotti, S. Matthies, and H. R. Wenk, IUCr: Newsletter of the CPD **21**, 14 (1999).

[21] N. C. Popa and D. Balzar, J. Appl. Crystallogr. **35**, 338 (2002).

[22] S. Matthies and M. Humbert, Phys. Status Solidi B **177**, K47 (1993).

[23] S. Matthies, H. G. Priesmeyer, and M. R. Daymond, J. Appl. Crystallogr. **34**, 585 (2001).

[24] B. B. Karki, R. M. Wentzcovitch, S. de Gironcoli, and S. Baroni, Science **286**, 1705 (1999).

[25] A. K. Singh, J. Appl. Phys. **73**, 4278 (1993).

[26] A. K. Singh, J. Phys. Chem. Solids **65**, 1589 (2004).

[27] M. R. Lee, P. A. Bland, and G. Graham, Mineral. Mag. **67**, 581 (2003).

[28] M. H. F. Overwijk, F. C. van den Heuvel, and C. W. T. Bulle-Lieuwma, J. Vac. Sci. Technol. B **11**, 2021 (1993).

[29] M. W. Phaneuf, Micron **30**, 277 (1999).

[30] R. Wirth, Eur. J. Mineral. **16**, 863 (2004).

[31] P. Pradère, J. F. Revol, L. Nguyen, and R. St. John Manley, Ultramicroscopy **25**, 69 (1988).

[32] P. Pradère and E. L. Thomas, Ultramicroscopy **32**, 149 (1990).

[33] S. V. Sinogeikin and J. D. Bass, Phys. Earth Planet. Inter. **120**, 43 (2000).

[34] C. H. Whitfield, E. M. Brody, and W. A. Bassett, Rev. Sci. Instrum. **47**, 942 (1976).

[35] A. E. Gleason, H. Marquardt, B. Chen, S. Speziale, J. Wu, and R. Jeanloz, Geophys. Res. Lett. **38**, L03304 (2011).

[36] H. Marquardt, S. Speziale, H. J. Reichmann, D. J. Frost, F. R. Schilling, and E. J. Garnero, Science **324**, 224 (2009).

[37] R. Chaim, J. Mater. Res. **12**, 1828 (1997).

[38] Y. Zhou, U. Erb, and K. T. Aust, Philos. Mag. **87**, 5749 (2007).

[39] S. Speziale and T. S. Duffy, Phys. Chem. Miner. **29**, 465 (2002).

[40] G. F. Davies, J. Phys. Chem. Solids **35**, 1513 (1974).

[41] G. F. Davies and A. M. Dziewonski, Phys. Earth Planet. Inter. **10**, 336 (1975).

[42] R. Hill, Proc. Phys. Soc. London, Sect. A **65**, 349 (1952).

[43] F. Li, Q. Cui, Z. He, T. Cui, C. Gao, Q. Zhou, and G. Zou, Appl. Phys. Lett. **88**, 203507 (2006).

[44] H. S. Lim, M. H. Kuok, S. C. Ng, and Z. K. Wang, Appl. Phys. Lett. **84**, 4182 (2004).

[45] M. H. Kuok, H. S. Lim, S. C. Ng, N. N. Liu, and Z. K. Wang, Phys. Rev. Lett. **90**, 255502 (2003).